Influence of vortex models on the prediction of 2D airfoil vortex interaction

S. Loiodice, D. Drikakis, A. Kokkalis

Aerospace Sciences Dept., School of Engineering, Cranfield University, Cranfield MK43 0AL

Abstract

Four different semi-empirical vortex models, namely the Rankine, Taylor, Scully and Vatistas vortices are applied to the analysis of airfoil-vortex interaction in order to understand their effect on the aerodynamic and aeroacoustic predictions. Two interaction problems are analysed, considering the NACA0012 airfoil first in subcritical and then in supercritical conditions. The aerodynamic analysis is performed using an Euler solver with a second order upwind finite-volume scheme in space and second order accurate implicit time integration using dual time-step sub-iteration. The aeroacoustic predictions are obtained using a permeable surface integral formulation of the Ffowcs Williams-Hawkings equation. The effects of the different vortex models are compared by calculating the ΔP field, which is the difference between two vortex induced pressure fields.

Key words: CFD, Aeroacoustics, Scully, Vatistas, Rankine, Taylor, Vortex, FW-H equation

1. Introduction

Various semi-empirical vortex models are exploited in aerodynamics applications. Yet, researchers are still focusing on the optimisation of the existing models or on creating novel models with increased capabilities for capturing the complex vortical structures of the vortices observed during experiments.

Semi-empirical vortex models are required during both experimental campaigns and computational analyses. Bagai and Leishman, [1], proposed the use of density gradient methods which combined with semi-empirical vortex models allow to obtain analytic results for the contrast variation of two dimensional compressible vortices. The mathematical results are strongly dependant on the particular choice of the vortex model.

On the computational side, extensive use of potential codes combined with wake simulation and semi empirical vortex models have enhanced the accuracy of aerodynamic predictions for fixed and rotary wing aircrafts. In particular, during the last two decades, the introduction of comprehensive codes has greatly improved aerodynamics and aeroacoustics predictions for helicopter rotors. In fact, these tools are capable of resolving the coupling of aeroelasticity and aerodynamics, which drives the complex aeromechanics of helicopter rotors.

Currently most of the comprehensive codes implement free wake simulation as opposed to the less accurate prescribed wake. While the latter method makes assumptions on the rotor wake geometry, the free wake simulation computes the complete wake geometry by mean of time marching algorithms which update the wake shape and position at every time step.

Although comprehensive tools which exploit the free wake analysis have higher accuracy, they can still present instabilities when the wake panels approach body surface control points. The instabilities are mainly due to unrealistic modelling of the

Blade Vortex Interaction (BVI) physics when a zero-thickness wake is used, and can be avoided using thick vortices with semi-empirical models for the vortex core. A non-zero thickness wake is essential during vortex body interaction because the local fluid flow around the impact region is determined by the spatial distribution of vorticity. Furthermore, the use of finite thickness vortex cores allows the calculations of Blade Wake Interaction phenomena such as the interactions between two close blade trailing vortices.

Hence, semi-empirical vortex models play a major role in order to obtain a more accurate and realistic modelling of a close interaction between wake and body. In fact in recent years, more sophisticated wake simulation and blade tip vortex models have been implemented in comprehensive codes with the aim of further improving the overall predictions [2]. On the other hand, the numerical or analytical solutions of 3-D unsteady Navier-Stokes equations to describe the tip vortex are not feasible. Therefore, in many engineering aerodynamic computations free-wake simulation with algebraic semi-empirical vortex models are used.

It is important to highlight that the particular choice of wake simulation and vortex model exploited in the aerodynamic calculations influences the quality of the computed predictions. In case of aeroacoustic modelling of the noise generation a possibly stronger influence was identified by Baghwat et al. [3]. In fact, vortex models differ not only with respect to the tangential and axial velocity distributions but also in the density and pressure field which they produce. Such differences could be considered to have negligible influence on aerodynamic calculations, however they will certainly have effect on aeroacoustic predictions.

Vatistas et al., [4], pointed out the lack of knowledge about noise generated by the deforming vortices during vortex body interactions. They presented the different effects produced by two semi-empirical vortex models, the Taylor vortex and the Vatistas n=2 vortex, applied to two theoretical types of vortex body interaction: vortex impinging on a flat plate and on a circular cylinder.

The aim of this article is to identify the effects of different vortex models on both aerodynamic and aeroacoustic calculations of vortex body interactions. In fact, helicopter rotors BVI is a particular and interesting case of vortex body interaction because it is one of the most annoying sources among helicopter's rotor noise during approach.

Furthermore, the noise produced by helicopter rotors during BVI depends on the strength of the blade tip vortices, the vortex core size, the interaction angles and vertical separation between the vortex and the blade, labelled as miss distance. BVI noise is therefore among all the helicopter rotor noise sources the one which is most influenced by the particular choice of rotor wake simulation and tip vortices models.

Given the importance of BVI noise, in this paper the attention is focused on the effect of different vortex models on a two dimensional version of this phenomenon: airfoil-vortex interaction. This is in fact a representative case which has similar characteristics with respect to the three dimensional BVI phenomenon and has a simple two dimensional geometry.

The comparisons will focus on the differences induced by the vortex models and will help to better understand the influence of the vortex models on the density and pressure distribution during noise generation phenomena due to vortex-body interaction. In section 2 are described the four semi-empirical vortex models considered in the present analysis along with their mathematical formulations. It follows in section 3 the description of the numerical method exploited for the aerodynamic calculations and the results obtained with this analysis. The conclusions are then presented in section 4.

2. Vortex Models

Several semi-empirical models have been developed, first by Rankine,[5], Lamb and Oseen, [7], then by Taylor, [6] and more recently by Vatistas, [8], which proposed a family of self similar vortices comprising some of the previous existing models.

The most exploited vortex profiles in aerodynamic predictions are certainly the Scully model, the Lamb-Oseen, and the Rankine vortex profile. Baghawt and Leishman, [3], demonstrated that the Lamb-Oseen model can be closely approximated using the self similar vortex family of Vatistas with $n = 2$. In fact, in this article this latter vortex model will be considered in place of the Lamb-Oseen model, and the different effects of all the aforementioned models will be analysed.

Up to now, the various vortex models have only been mentioned by name with no details of their mathematical representation. This is carried out in the following sections where descriptions of the an-

alytical formulas for the velocity, density and pressure profiles of each vortex core model considered in this study are presented.

A generic vortex model is given as a tangential velocity distribution which is only a function of the distance from the vortex core centre and which can be written in polar coordinates as:

$$v_\theta = v_\theta(r, \Gamma, R_c) \tag{1}$$

$$v_r = 0 \tag{2}$$

Where Γ represents the total circulation of the vortex, defined as $\Gamma = \int \Omega \mathrm{d}r\mathrm{d}\theta$ (Ω is the vorticity) and R_c is the vortex core radius. With the assumption, eq.(1), that the velocity profile is only a function of r, it is possible to obtain an expression for the pressure field induced by the vortex from the momentum equations in polar coodinates:

$$\frac{\partial p}{\partial r} = \rho \frac{v_\theta^2}{r} \tag{3}$$

$$\frac{\partial p}{\partial \theta} = 0 \tag{4}$$

which means that $p = p(r)$ Considering a compressible fluid in isoentropic condition, the pressure field is connected to the density field by mean of the following relation:

$$\frac{p}{\rho^\gamma} = \frac{p_\infty}{\rho_\infty^\gamma} \tag{5}$$

The above relation leads to the definition of the constant $k_0 = \frac{p_\infty}{\rho_\infty^\gamma}$, and can be used in eq.(3) to obtain the following differential equation for ρ:

$$\frac{1}{\rho}\frac{\mathrm{d}\rho}{\mathrm{d}r} = \frac{\rho_\infty}{\gamma p_\infty}\frac{v_\theta^2}{r} \tag{6}$$

Eq.(5) and (6) can be used to obtain the pressure and density filed for every semi-empirical vortex model.

The Taylor vortex model, a compact vortex, has been proposed by Taylor, [6], and used by many authors including Vatistas et al., [4] and Colonius et al., [10]. The tangential velocity distribution of the Taylor vortex has the following expression:

$$v_\theta = v_{\theta max}\frac{r}{R_c} e^{\left(\frac{1-\left(\frac{r}{R_c}\right)^2}{2}\right)} \tag{7}$$

where $v_{\theta max}$ is the maximum tangential velocity and R_c is the radius of the vortex core, corresponding to the maximum tangential velocity.

Integrating Eq.(6), the density and pressure distribution for the Taylor vortex are given by:

$$\rho(r) = \rho_\infty \left[1 - \frac{v_{\theta max}^2}{k_0}\frac{\gamma - 1}{2} e^{\left(1-\left(\frac{r}{R_c}\right)^2\right)}\right]^{\frac{1}{\gamma-1}} \tag{8}$$

$$p(r) = k_0 \rho^\gamma \tag{9}$$

Scully at al., [9], defined a vortex velocity profile in the following form:

$$v_\theta = V_\Gamma \frac{\overline{r}}{\left(1 + \overline{r}^2\right)} \tag{10}$$

where $\overline{r} = \frac{r}{R_c}$ and $V_\Gamma = \frac{\Gamma}{2\pi R_c}$.

It is possible, by defining $\zeta = \frac{V_\Gamma^2}{2k_0}$, to write the density and pressure field for the Scully vortex in a compact form:

$$\rho(r) = \rho_\infty \left[1 - \zeta\left((\gamma - 1)\frac{1}{1 + \overline{r}^2}\right)\right]^{\frac{1}{\gamma-1}} \tag{11}$$

$$p(r) = k_0 \rho^\gamma \tag{12}$$

Recently Vatistas, [8], proposed a family of algebraic vortex velocity profiles, comprising some of the aforementioned models, which can be written in the form:

$$v_\theta = V_\Gamma \frac{\overline{r}}{\left(1 + \overline{r}^2\right)^{\frac{1}{n}}} \tag{13}$$

The exponent n can vary from $n = 1$ to $n = \infty$. It is obvious that for $n = 1$ the profile coincides with the Scully model. As discussed above, the Vatistas vortex with $n = 2$ will be analysed in this paper.

The following assumptions are made in order to compare the effects of the different models on the numerical predictions:

– the same vortex core radius R_c is used for all the vortex models
– the same total circulation Γ is used in every model

In particular two different values of R_c are used during the calculations, $R_c = .018c$ and $R_c = .05c$ where c is the airfoil chord. For the smaller R_c $\Gamma = .283$ while for the other case $\Gamma = .2$. It must be noticed that fixing the two model's parameters R_c, Γ produces different maximum tangential velocities for each vortex model, this is visible in Fig.1. In this figure the tangential velocities are non-dimensionalised using V_γ which is constant for a given R_c, Γ. The maximum tangential velocity for Taylor and Rankine vortices is equal to 1, while the maximum velocity for Vatistas vortex is equal to 0.74 and for Scully is 0.5. From the figure is also

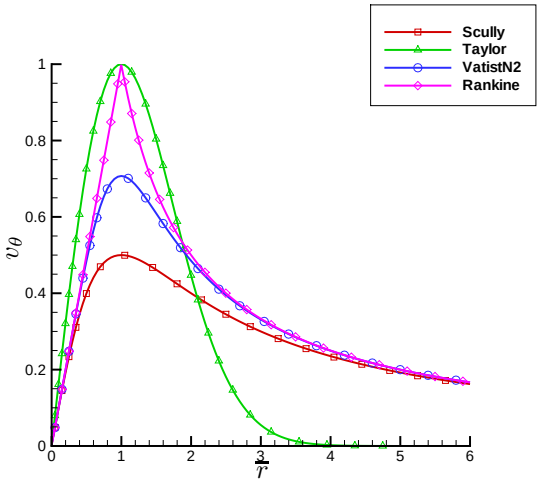

(a) ***Velocity profiles***

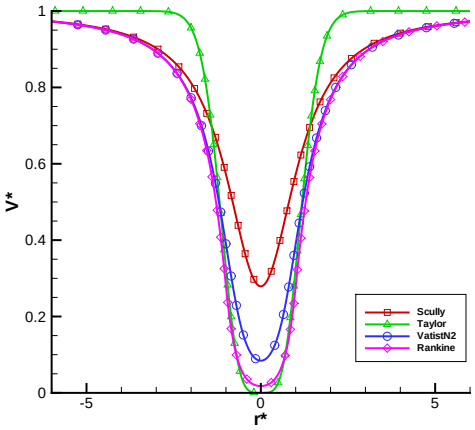

(b) ***Density profiles***

Fig. 1. Vortex-induced profiles

clear that the Taylor vortex velocity profile influences only a very compact zone within the limit of $\overline{r} = 4$. The behaviour is similar also for pressure and density distributions where the peaks of Taylor and Rankine vortices are much higher compared to the other models.

3. Results and Discussion

3.1. *Numerical method*

Vortex body interaction is one of the most challenging problems for aerodynamic and aeroacoustic prediction. For instance, in the case of airfoil-vortex interaction, different levels of numerical approximation, [12], [13], [14], have been adopted depending on the computational resources and flow discretisations. Several difficulties arise during numerical prediction of vortex body interaction. The main problem encountered is the numerical dissipation which characterises CFD codes. This severely affects the strength of the vortices, particularly in the flow regions where the grid resolution is low, such as far away from the airfoil.

In the present study, the two-dimensional implicit Euler solver of the commercial software Fluent was exploited. The Euler solver is based on a cell centred finite volume method with Roe Flux-Difference Splitting (FDS) scheme for the convective fluxes. The governing equations are integrated in time using an second order implicit time-marching method with dual time stepping. The inner iterations of the dual time stepping were performed until residual convergence dropped by three orders of magnitude.

A second order upwind scheme was used for the spatial discretisation. In order to limit the numerical dissipation which is induced by large cells, three different meshes levels have been tested during this study. In effect, as discussed above, researchers have tried to resolve the dissipation problem by means of several different techniques such as Compressible Vorticity Confinement (CVC), [13] or Adaptive Algorithms, [12] and [14]. These efforts were aimed at defining a method which allows to use larger mesh cells, and hence less computational resources.

In the present paper the efficiency of the mesh distribution and the CFD algorithm were not the main concern. The three meshes considered have a number of nodes varying from 100 up to 210 thousand, and after a comparison of the preserved vortex strengths, the finer mesh was chosen for all the calculations. This latter mesh is shown in Fig.2, where the two blocks used can be observed, with a very fine mesh upstream of the airfoil leading edge. The two blocks are connected using non-conformal interfaces which allows the use of a different node distribution on each side of the faces connecting the two blocks.

3.2. *Subcritical Head-on Interaction*

Airfoil-vortex interaction has been studied by various researchers and the experiment conducted by Lee and Bershader, [11], is a well documented example. During the experimental campaign the authors studied a head-on parallel interaction with a $M_\infty = 0.5$ and non-dimensionalised $\Gamma = 0.283$ and

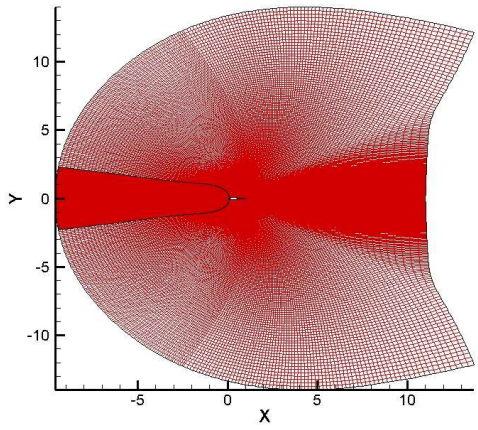

(a) *Overall*

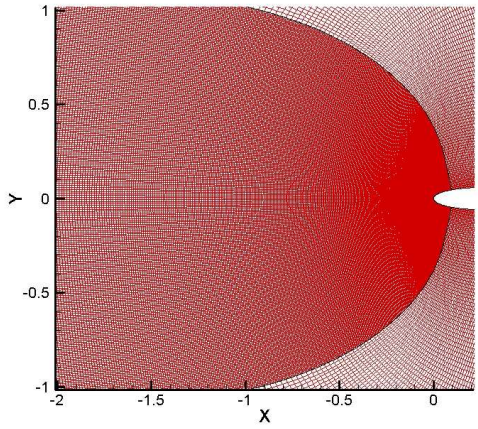

(b) *Close up*

Fig. 2. Mesh used during calculations

$R_c = 0.018$. In the head-on case the miss distance between the airfoil leading edge and the centre of the vortex core is 0.

This experiment is of particular significance since it was used as a reference case for previous computational analyses, [12],[13],[14]. All these numerical analyses were conducted by superimposing the Scully semi-empirical vortex model to a steady solution of the flow around the NACA 0012 airfoil with the same flow conditions as in [11]. To the knowledge of the authors, no numerical study exploited a vortex model other than the Scully model for this particular analysis.

The unsteady Euler calculations for this case have been performed adopting the numerical method described in the previous section with a physical time step size of $\delta t = 0.01$ non-dimensionalised by the time $t_c = c/U_\infty$, i.e. the time that a signal travelling with the free stream velocity needs to cover one airfoil chord length c. This means that the vortex, which is convected by the free stream velocity, was moving every time step of $\delta x_v = 0.01c$, which in this case is approximately half the core radius, $\delta x_v \approx R_c/2$.

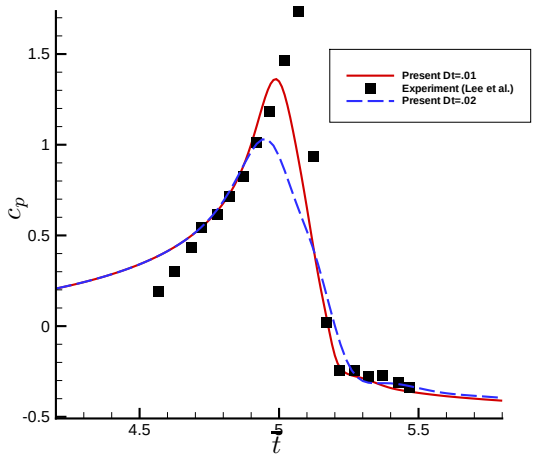

(a) c_p *Upper surface*

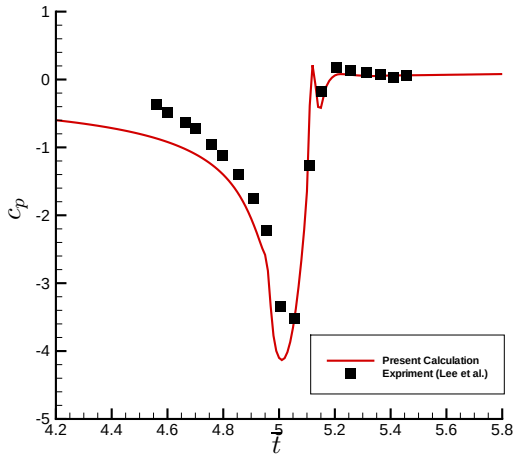

(b) c_p *Lower surface*

Fig. 3. c_p time history at the point $x = 0.02c$ and comparison with the experiment of Lee et al., [11]

The comparisons of the pressure coefficient c_p time history with the experimental data in [11], are shown in Fig.3. The plots refer to the case subcrit-

ical Head-on interaction with $M_\infty = 0.5$ and are calculated in the point $x = 0.02c$, i.e. 2% from the airfoil leading edge (L.E.). It is interesting to see the effect of time step size on the calculations, in Fig.3(a). In particular, by using a larger Δt, the c_p peak value over both lower and upper surfaces of the airfoil, is underestimated of around 50%.

The differences in pressure fields induced by the Scully and Vatistas models are presented in Fig.4 and Fig.5. In particular, these figures show contours of the pressure difference DP at four different positions of the vortex, starting from the point where the vortex was initially superimposed to the steady solution, 4(a). The contours in this case have been clipped to $20Pa$, i.e. the regions in red, such as the vortex core, have higher differences.

From the plots is clear that the initial pressure field difference, Fig.4(a), when the two vortex are superimposed, is concentrated just in the region of the vortex cores, with some scattering from the airfoil leading edge. The vortex is then convected with $M_\infty = 0.5$ and when it reaches a distance of 2 chords from the leading edge, Fig.4(b), the pressure field difference, which is emitted by the centre of the vortex core at $M = 1$, has now a radius of 2 chords, i.e. $1/(M_\infty)$ times the distance travelled by the vortex. The ΔP field now reaches the airfoil leading edge and the region in proximity of the airfoil is altered by the presence of the solid body.

Following the vortex further downstream at 1 chord distance from the L.E., Fig.5(a), the ΔP field has now a radius of 4 chords and the airfoil is fully immersed. The side of the ΔP field containing the airfoil is visibly different from the clean side. A part from the alteration induced by the airfoil solid surfaces, it is quite evident the presence of a scattered ΔP wave from the airfoil leading edge which was generated when the ΔP field reached the L.E., and its centre is now convected downstream of 1 chord with a radius of 2 chords. This scattered wave tends to eliminate the ΔP difference along its wave front which in fact can be recognised by the darker colour circle centred in the airfoil trailing edge (T.E).

A very similar behaviour can be recognised in Fig.5(b), but in this case the vortex has reached the airfoil L.E. and the ΔP field in proximity of the airfoil surface has large magnitude, indicated by the dark red region enclosing the airfoil. The wave front of the ΔP field extends now in a radius of 6 chords around the airfoils L.E., where the vortex is now positioned.

The figures 4(b),5(a) and (b) show clearly visible

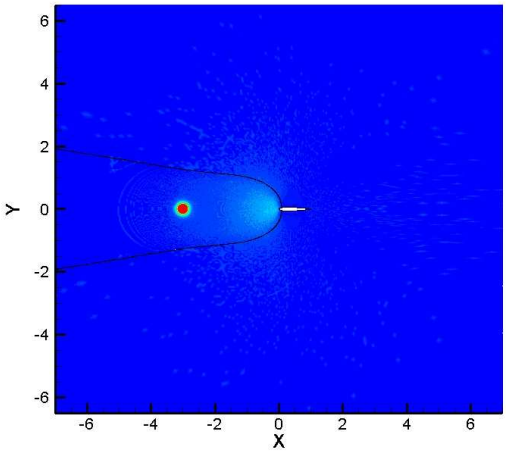

(a) $x_v = -3c$

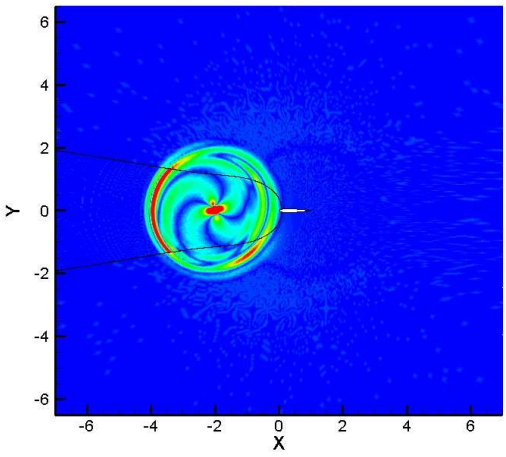

(b) $x_v = -2c$

Fig. 4. Difference in pressure filed between Scully and Vatistas models, for different positions of the impinging vortex.(The contours are clipped [0-20]Pa)

four spirals staring from the vortex centre and extending up to the ΔP wave front. These are generated by the rotational movement of the vortex due to its tangential velocity, and the lengths of the spirals depend on differences in the vortex-induced velocity fields of the two vortex models, shown in Fig.1(a).

Figure 6, shows the comparison between the pressure field induced by the Scully, Vatistas and Rankine models. The ΔP magnitudes are much higher than Fig.4, visible as the red colour regions, and the differences between Rankine and Scully are much

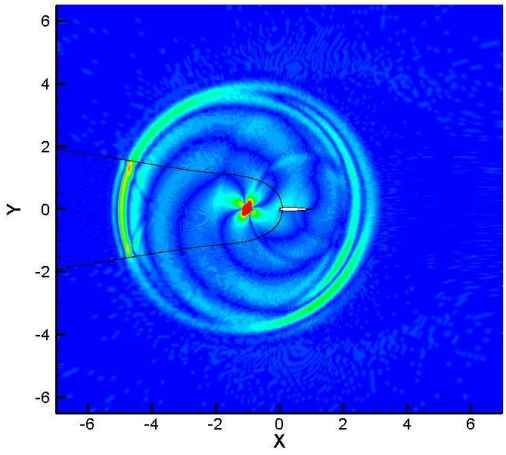

(a) $x_v = -1c$

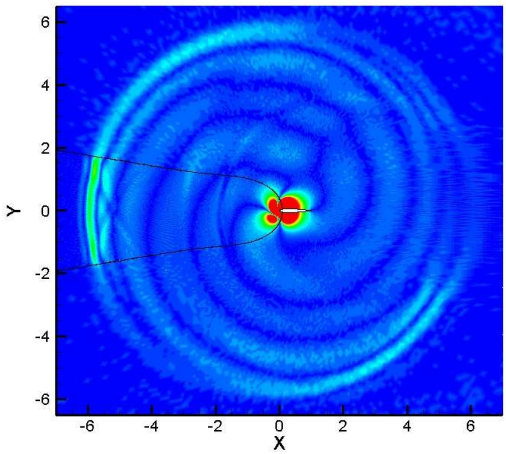

(b) $x_v = 0c$

Fig. 5. Difference in pressure filed between Scully and Vatistas models, for different positions of the impinging vortex.(The contours are clipped [0-20]Pa)

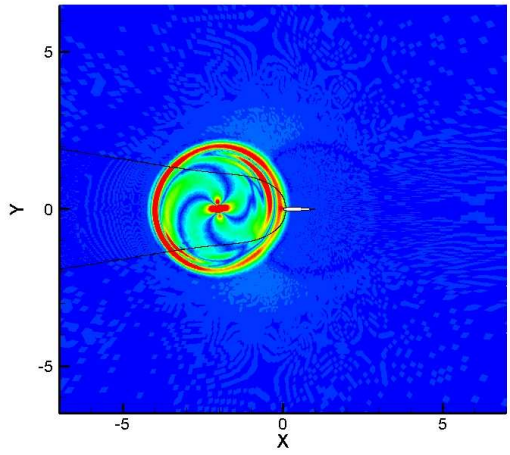

(a) ΔP ***Scully-Rankine***

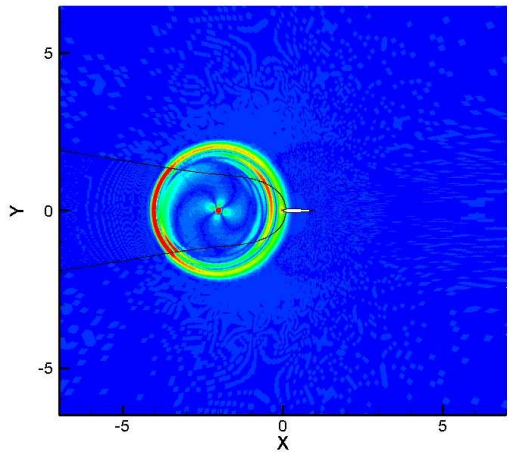

(b) ΔP ***Vatistas-Rankine***

Fig. 6. ΔP differences between three vortex models, (Contours clipped [0-20]Pa, $x_v = -2c$)

larger than Rankine-Vatistas, as could be expected from the equations of the models. The behaviour of the ΔP is similar to the one described above and the spirals are more intense in the Scully Rankine comparison. Furthermore, the spirals' lengths are longer in the latter case since the difference between the maximum tangential velocities for Rankine-Scully models are larger than Rankine-Vatistas ones.

It must be noted that even if the Vatistas and Scully models belong to the same family and the Rankine has a very similar equation, the ΔP fields are of considerable magnitude when compared with the human hearing threshold $2\mu Pa$. When considering the Taylor model, which has a different mathematical form, the ΔP field becomes even more intense. In figure 7 the contour range has been extended up to $2kPa$, i.e. 100 times the one used in figure 4.

3.3. *Supercritical Parallel Interaction*

The case presented above was an Head-on interaction and the vortex was convected with a subcrit-

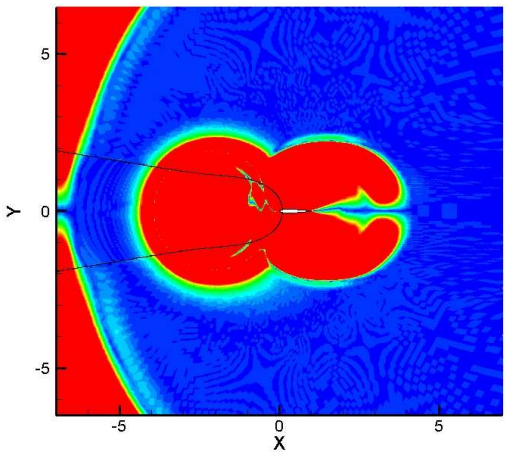

(a) ***Contours*** $(0-20)Pa$

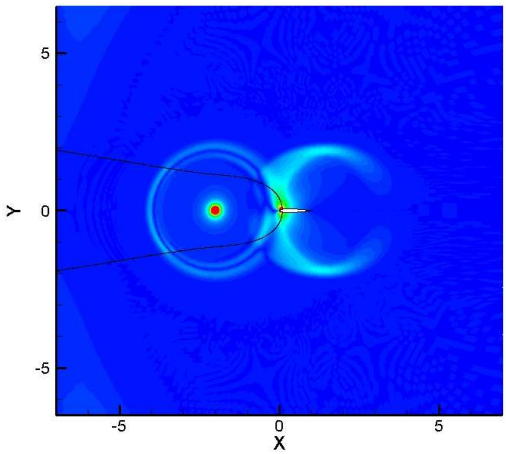

(b) ***Contours*** $(0-2000)Pa$

Fig. 7. ΔP differences between Taylor and Scully models, ($x_v = -2c$)

ical Mach number. In the following case $M_\infty = 0.8$ and the vortex has a miss distance from the L.E. of $y_v = 0.25c$. The parameters for the vortex models are: non-dimensionalised $\Gamma = 0.2$ and $R_c = 0.05$, as in [12],[14] and [15]. Since the Mach is supercritical, two shocks are present in the steady state solution of the $NACA0012$. This means that the airfoil vortex interaction is further complicated by the interaction of the vortex with the shocks. In effect, the presence of the shocks influences the ΔP field as shown in Fig.8, where the maximum pressure contour was kept 20 Pa for consistency with the previous plots. The scattered waves are now 3, one from the L.E. and one from each of the shocks. Furthermore the ΔP magnitude is much higher than for the subcritical case and the shocks position and magnitude are affected by the differences in the models.

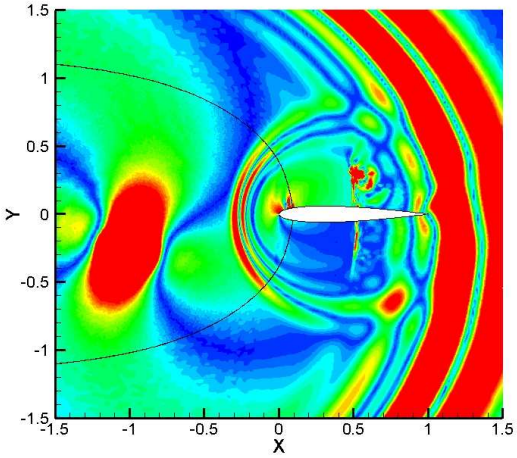

Fig. 8. ΔP differences between Scully and Vatistas models, ($M_\infty = 0.8$, $x_v = -1c$, Contours $(0-20)Pa$)

3.4. *Acoustic Pressures*

The near-field ΔP differences between the vortex models have been presented in the previous section. From the discussion and by analysing the contour plots, it appears that the differences between the models are smoothed during the propagation. Hence, it is necessary to analyse the far-field acoustic pressure in order to understand wether the smoothing is due to the intrinsic dissipation of the CFD or to the physical dispersion of the pressure signal.

In the present study the far-field acoustic pressure is predicted using an in-house aeroacoustic code, [2], based on the Ffowcs Williams-Hawkings equation on permeable surfaces. Three observer position have been considered, $5c$, $10c$ and $20c$ above the airfoil. The analysis is focused on the subcritical head-on case which presented a lower ΔP magnitude and hence weaker front waves, Fig.5(b). The acoustic pressure time history at an observer $y_o b = 20c$ above the airfoil is shown in Fig.9.

The differences in the far field acoustic pressure between the Vatistas and the Scully Vortex models are presented in Fig.10. Obviously the closest observer perceives the higher pressure differences,

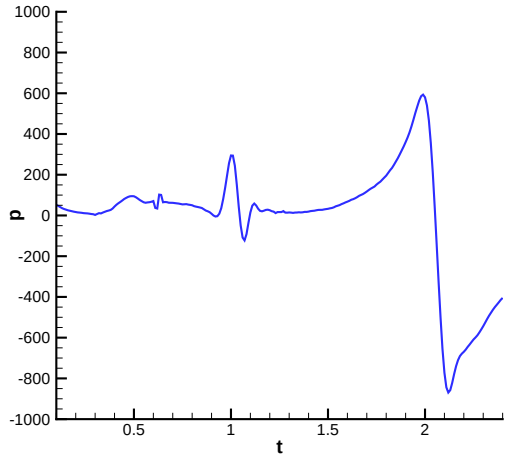

Fig. 9. Far field Acoustic Pressure, $y_{ob} = 20c$

Fig.10(a), in the range of $150Pa$. This value goes down about 50% for the observer in $y_{ob} = 10c$, Fig.10(b), where it is also visible a shifting of the signal pattern takes place. It is possible that this shifting is due to the differences in the tangential velocities between the two vortex models.

Moving further away from the airfoil, an observer positioned at $y_{ob} = 20c$, Fig.10(c) perceives a ΔP signal which has half the magnitude of the one in Fig.10(b) and one quarter of the amplitude reaching the observer in $y_{ob} = 5c$, Fig.10(a). This trend suggests a linear behaviour, i.e. the amplitude of the acoustic signal decays as the inverse of the radiation distance, as expected from the theory. Hence the excessive decay presented in Fig.5 must be attributed to the intrinsic numerical dissipation. It must be highlighted that the initial difference in the induced pressure fields is contained only in the vortex core, which in the case under analysis is 0.0184 chords. This means that the initial pressure difference can be perceived in a region of $1000R_c$, at the observer $y_{ob} = 20c$.

4. Conclusions

Four different semi-empirical vortex models have been applied to studdy the pressure field variation due to an airfoil-vortex interaction. It is clear from this study, that the ΔP field is non negligible both for low and high Mach number cases. ΔP is clearly more intense for supercritical conditions and is strongly dependant upon the different vortex

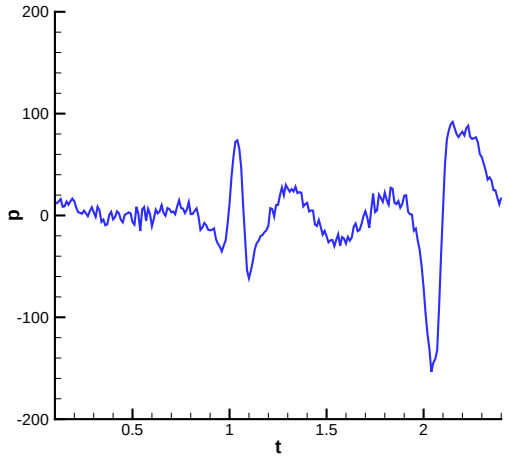

(a) $y_{ob} = 5c$

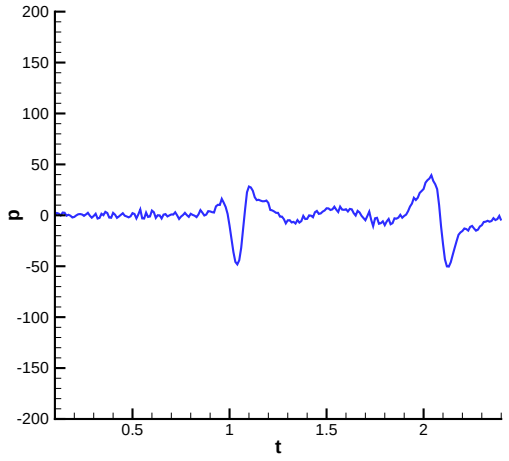

(b) $y_{ob} = 10c$

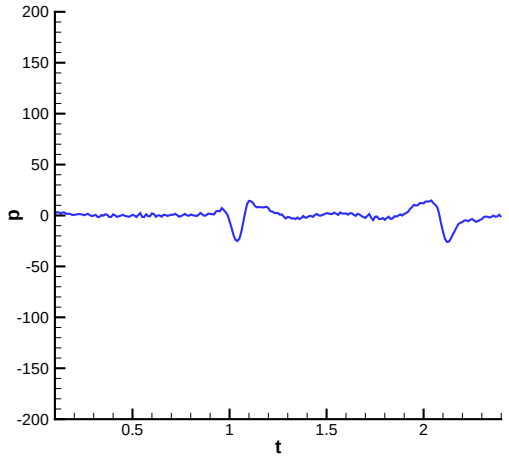

(c) $y_{ob} = 20c$

Fig. 10. Differences in the far field acoustic pressure between Vatistas and Scully models for three observer positions

mathematical formulations, such as the Taylor and the Scully. The contour plots of the ΔP field reveal the motion of the pressure waves induced by the vortices and by the presence of discontinuities such as shocks or solid walls.

The aeroacoustic analysis has shown that the ΔP differences could be underestimated by the aerodynamic calculations due to the large numerical diffusion which weakens the ΔP wave fronts. Furthermore, the differences in the far-field acoustic pressures cannot be neglected even for an observer at large distance. Hence these differences must be taken into account when comparing aeracoustic predictions obtained by exploiting different vortex models.

5. Acknowledgments

This work is supported by the European Union under the 6th Framework Programme for Research and Technological Development, Friendcopter project.

References

[1] Bagai, A.; Leishman, J.G. *Flow visualization of compressible vortex structures using density gradient techniques*, Experiments in Fluids Vol. 15, pp. 431-442, 1993

[2] Loiodice, S.; Kokkalis, A.; Drikakis, D.; Perez, G.; Ponza, R.; Bernardini, G. *Assessment of computational tools for the prediction of BVI noise*, Proccedings of the 32nd European Rotorcraft Forum, Maastricht, Netherlands, 2006.

[3] Baghwat, M. J.; Leishman, J.G. *Generalised viscous vortex model for application to free-vortex wake and aeroacoustic calculations*,in: Proceedings of the Annual Forum of the American Helicopter Society, Montreal, Canada, 2002.

[4] Povitsky, A.; Zheng, T.; Vatistas, G.H. *Effect of vortex profile on sound generation in a non-uniform flow* Mathematics and Computers in Simulation,Vol. 65 , no.4-5, pp.447-468, May 2004

[5] Rankine, W.J.M., *Manual of Applied Mechanics*, C. Griffen Co., London, 1858

[6] Taylor, G.I., *On the Dissipation of Eddies*, The Scientific Papers of Sir Geoffrey Ingram Taylor, vol. 2, 1958, pp. 96-101.

[7] Lamb, H., *Hydrodynamics*, 6th ed., Cambridge University Press, Cambridge, UK,1932

[8] Vatistas, G.H., *New Model for Intense Self-Similar Vortices*, J. Propul. Power Vol. 14, no. 4, pp. 462-469, 1998

[9] Scully, M. P.; Sullivan,J. P., *Helicopter Rotor Wake Geometry and Airloads And Development of Laser Doppler Velocimetry for Use in Rotor Wakes*, Massachusetts Institute of Technology, Aerophysics Laboratory, Technical Report 183, August 1972

[10] Colonius, T.; Lele, S.K.; Moin, P. *The scattering of sound waves by a vortex: numerical simulations and analytical solutions*, J. Fluid Mech. Vol. 260, pp. 271-298, 1994

[11] Lee, S.; Bershader, D. *Head-on parallel blade-vortex interaction*, AIAA Journal,Vol. 32, no. 1, pp. 16-22. Jan. 1994

[12] Tang, L.; Baeder, J. D., *Adaptive Euler Simulations of Airfoil-Vortex Interaction*, Int. J. Numer. Meth. Fluids, Vol. 53, pp.777-792, 2007

[13] Morvant, R.; Badcock, K. J.; Barakos, G. N.; Richards, B. E., *Airfoil-vortex interaction using the compressible vorticity confinement method*, AIAA Journal. Vol. 43, no. 1, pp. 63-75. Jan. 2005

[14] Oh, W. S.; Kim, J. S.; Kwon, O. J., *Numerical simulation of two-dimensional blade-vortex interactions using unstructured adaptive meshes*, AIAA Journal. Vol. 40, no. 3, pp. 474-480. Mar. 2002

[15] Srinivasan, G. R.; and McCroskey, W. J.; *Numerical Simulations of Unsteady Airfoil-Vortex Interactions*, Vertica, Vol. 11, no. 1, pp. 3-28, 1987